



**HAL**  
open science

## Interpretable crack features for the representation of kinematic fields in the case of fatigue overloads

Ghita Bahaj Filali, Michel Coret, Adrien Leygue, Julien Réthoré

### ► To cite this version:

Ghita Bahaj Filali, Michel Coret, Adrien Leygue, Julien Réthoré. Interpretable crack features for the representation of kinematic fields in the case of fatigue overloads. 2024. hal-04496354v1

**HAL Id: hal-04496354**

**<https://hal.science/hal-04496354v1>**

Preprint submitted on 8 Mar 2024 (v1), last revised 3 Oct 2024 (v2)

**HAL** is a multi-disciplinary open access archive for the deposit and dissemination of scientific research documents, whether they are published or not. The documents may come from teaching and research institutions in France or abroad, or from public or private research centers.

L'archive ouverte pluridisciplinaire **HAL**, est destinée au dépôt et à la diffusion de documents scientifiques de niveau recherche, publiés ou non, émanant des établissements d'enseignement et de recherche français ou étrangers, des laboratoires publics ou privés.



Distributed under a Creative Commons Attribution 4.0 International License

1 Interpretable crack features for the representation  
2 of kinematic fields in the case of fatigue overloads

3 Ghita BAHAJ FILALI<sup>1\*</sup>, Michel CORET<sup>1†</sup>, Adrien LEYGUE<sup>1†</sup>,  
4 Julien RETHORE<sup>1†</sup>

5 <sup>1\*</sup>Nantes Université, Ecole Centrale Nantes, CNRS, GeM, UMR 6183,  
6 [F-44300] , France.

7 \*Corresponding author(s). E-mail(s): [ghita.bahaj-filali@ec-nantes.fr](mailto:ghita.bahaj-filali@ec-nantes.fr);

8 Contributing authors: [michel.coret@ec-nantes.fr](mailto:michel.coret@ec-nantes.fr);  
9 [adrien.leygue@ec-nantes.fr](mailto:adrien.leygue@ec-nantes.fr); [julien.rethore@ec-nantes.fr](mailto:julien.rethore@ec-nantes.fr);

10 †These authors contributed equally to this work.

11 **Abstract**

12 **Background:** many engineering structures are subjected to variable amplitude  
13 loading. A number of studies investigate the effects of post overload, even-though  
14 it is crucial to describe what occurs during the overloading. To the authors knowl-  
15 edge the number of studies that describe the overloading effects are few to none.

16 **Purpose:** the aim of this paper is to provide effective independent descriptors  
17 based on a purely kinematic measurements.

18 **Methods:** fatigue tests were conducted on a SENT specimen. Investigating crack  
19 propagation was through direct measurements using Digital Image Correlation  
20 (DIC) and Linear Elastic Fracture Mechanics (LEFM) via Williams' series expansion.  
21 The higher terms in Williams' series expansion, referred to as crack features  
22 were analyzed in cycles with and without overload.

23 **Results:** in a case without overload, all features exhibit a proportional regime.  
24 Singular Value Decomposition (SVD) analysis confirms that a single feature is  
25 adequate to characterize the mechanism. In a cycle with overload, the regime  
26 changes during the overloading phase, making it a signature of this phase. In this  
27 case, the SVD analysis reveals that two descriptors are needed for these cycles. A  
28 subsequent analysis allows the definition of two physically interpretable features.

29 **Conclusion:** this work presents a robust method to identify, based on kinematic  
30 measurements and SVD analysis, independent descriptors for the processes that  
31 occur during a cycle with overload. \*

---

\*License: CC-BY @TheAuthors

## 33 1 Introduction

34 In engineering, the prediction of the service life of components and structures is neces-  
35 sary to ensure safety. Enhancing the capacity to withstand diverse loading conditions  
36 can be regarded as a primary focus of engineering research. Reflecting real-world and  
37 complex conditions, cyclic loading can be considered one of the most studied loading  
38 types. Such repeated cyclic loading can cause fatigue cracking within structural compo-  
39 nents. This phenomenon can be particularly challenging to predict and manage,  
40 making it a central concern in engineering disciplines [20, 15]. For most of these com-  
41 ponents, real loading cycles involve variable amplitude rather than constant amplitude  
42 loading. Hence the study of overloads is important to understand their signature.

43 The effects of single peak tensile overloads have already been widely investigated  
44 [19, 16, 14] as this form of loading may result in significant load interaction effects.  
45 Several mechanisms have been proposed, based on Linear Elastic Fracture Mechanics  
46 (LEFM), to explain crack growth retardation post overload. This include models  
47 based on residual stresses [13], crack closure [6], strain hardening [5], crack branching  
48 [18] and reversed yielding [12].

49 Fatigue life prediction in this case is complex because most of the studies used the  
50 empirical Paris' law [7]. This law establishes a direct correlation between the stress  
51 intensity factor ( $\Delta K$ ) as single crack feature and the crack growth rate per cycle  
52 ( $da/dN$ ), and has been widely applied to model fatigue crack growth during constant  
53 amplitude loading. However, the Paris' law exhibits several limitations, specifically  
54 it only models the stable crack propagation, and does not consider the stress ratio  
55 effects [17]. Many other fatigue crack propagation laws have been proposed to over-  
56 come the limitations of the Paris law and also to deal with variable amplitude loading  
57 [1]. The proposed fatigue models differ on the number of features involved and the  
58 number of parameters required to be identified through curve fitting.

59  
60 This work aims to provide independent kinematic descriptors for the mechanisms  
61 that occurs during the overload. For this purpose, local and direct optical measure-  
62 ments of the displacement fields obtained through digital image correlation (DIC)  
63 during overload are analysed through LEFM via Williams' series expansion. The Series  
64 coefficients provide a first set of kinematic crack features. These are then further  
65 reduced to two interpretable features using data analysis and dimensionality reductions  
66 tools. This paper is structured as follows: in section 2 we presented the experimen-  
67 tal set-up, including material, loading condition and specimen geometry. The DIC for  
68 measuring kinematic fields and Williams' series expansion are recalled. Crack features  
69 are presented in section 3 and then analyzed qualitatively in section 4. In section 5  
70 a quantitative, Singular Value Decomposition (SVD)-based, analysis was carried out.  
71 The last section is a summary of the presented study.

72 **2 Raw data**

73 **2.1 Fatigue test on a SENT specimen**

74 The specimen is made of Al-7%Si cast alloy with an average grain size of 150  $\mu\text{m}$ .  
75 Eutectic Si particles are dispersed in a globular shape obtained by coalescence fol-  
76 lowing heat treatment (the material is provided by Centre Technique des Industries  
77 Mécaniques CETiM). The elastic material properties are the Young's modulus ( $E$ ) of  
78 74 GPa and the Poisson's ratio ( $\nu$ ) of 0.3. Experiments are done on a Single Edge  
79 Notched Tension (SENT) specimen. The geometry is defined in Figure 1.

80 The fatigue test was conducted in mode I, the specimen contains an initial notch at the  
81 border perpendicular to the tensile axis. The initial length of the notch is  $a_0 = 3$  mm,  
82 then the crack propagates through the whole specimen, until complete failure. All  
83 experiments were performed using an electro magnetic machine (Instron ElectroPuls  
84 E10000) with a load cell of 10 kN maximum loading capacity and a frequency of  $f=20$   
85 Hz.

86 Preliminary experiments have been conducted leading to the choice of a cycling range  
87 between  $F_{\min}=1\text{kN}$  and  $F_{\max}=7\text{kN}$ . The choice of the overloading load was a com-  
88 promise between the maximum capacity of the machine and a significant overloading  
89 load, thus  $F_{\text{ovl}}=1.25F_{\max}$ .

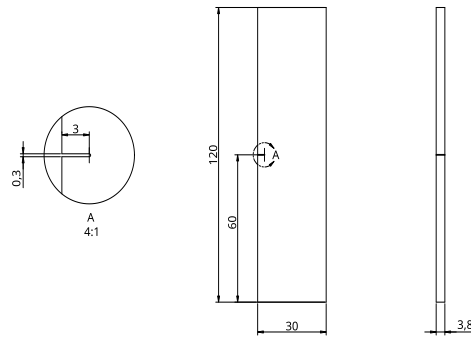


**Fig. 1:** SENT specimen geometry (dimensions in mm).

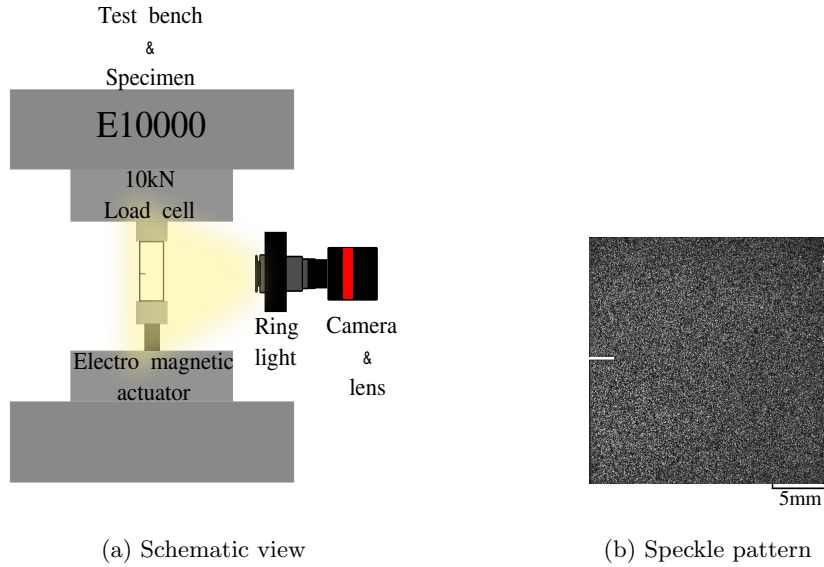


**Fig. 2:** Experimental setup

**Table 1** Optical system and patterning technique

Camera	47 Megapixel Vieworks
Image resolution	7920×6004
Lens	TOKINA 100 mm
Aperture	f/2.8
Field of view	38.7×23.3 mm
Image scale	1 pix = 4.8 $\mu$ m
Patterning technique	Spray paint (can + airbrush)

90 The experiment was divided into two stages:

- 91 • **Initiation.** The sample was subjected to cyclic tensile loading, the aim was to  
 92 achieve a crack length of 3 mm which was reached after 60000 cycles. This crack  
 93 length is sufficient to mitigate the influence of the notch during the initiation of the  
 94 crack.
- 95 • **Propagation plus overload stage.** After the pre-cracking stage, when crack prop-  
 96 agation was deemed sufficient, an overload was applied to the sample. Once the  
 97 crack has resumed growing, after 1000 cycles, the process of applying an overload  
 98 and letting the crack grow again afterwards is repeated until the sample breaks  
 99 (Figure 3).

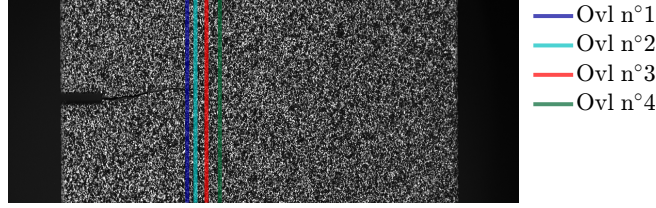


**Fig. 3:** Overload positions in the sample

100 During the experiment, pictures were taken for future DIC analyses. The images were  
 101 captured using a 47 Megapixels Vieworks camera equipped with a 100 mm lens (Tok-  
 102 ina). The lighting of the sample was ensured by a LED ring light (FPR-136BL2 by  
 103 CCS Inc). A black and white speckle pattern is painted on the specimen using cans  
 104 and an airbrush. The experimental setup can be seen in Figure 2, camera specifica-  
 105 tions are presented in Table 1.

106 An image of the unloaded and uncracked specimen is first taken. Then, during the pre-  
 107 cracking stage, images were captured each 5000 cycles at  $F_{\max}$ . During propagation  
 108 and overloading, images were taken each 0.5 kN from  $F_{\min}$  to  $F_{\max}$  and each 0.25 kN  
 109 from  $F_{\max}$  to  $F_{\text{ovl}}$  (Figure 4).

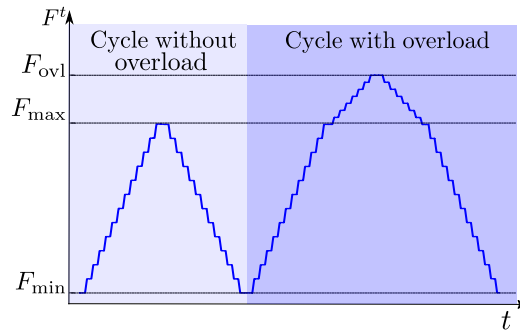


**Fig. 4:** Image acquisition strategy. Each image is taken at a constant force.

All the images taken during experiments were used for DIC processing. DIC is a full-field method that involves analysing a series of images to extract displacement fields. The displacement field  $\underline{u}_{\text{DIC}}$  is computed between an undeformed image  $I_0$  and a deformed one  $I_1$ . This displacement field is estimated following the optical flow equation 1:

$$I_0(\underline{X}) = I_1(\underline{X} + \underline{u}_{\text{DIC}}(\underline{X})). \quad (1)$$

110 The measurement of the displacement is an ill-posed problem. It is solved iteratively  
 111 in the least squares sense using a Finite Element (FE) discretization [2] implemented

112 in UFreckles software [11]. The displacement field is decomposed over a regular mesh  
 113 of 4-node bilinear quadrangular elements. A median filter with the 1<sup>st</sup> neighbours  
 114 was used to reduce the impact of noise (Table 2).  
 115

**Table 2** DIC software parameters

Software	UFreckles [11]
Shape function	Bi-linear quadrilateral Lagrange element (Q4P1)
Element size	[0.097 0.097] mm <sup>2</sup>
Post-filtering	Median filter using 1 <sup>st</sup> neighbours

## 116 2.2 Pre-overload and overload analysis

For all this study, cycles were analysed independently. For each cycle we computed the variation of the load related to  $F_{\min}$  as follows:

$$\delta_t F = F^t - F_{\min};$$

and the variation of the displacement field also related to the displacement at  $F_{\min}$  as follows:

$$\delta_t \underline{U} = \underline{U}^t - \underline{U}^{F_{\min}},$$

117 with  $\underline{U}^t$  and  $F^t$  is the  $t^{\text{th}}$  displacement vector and load respectively in the loading  
 118 range ( $F_{\min} \leq F^t \leq F_{\text{ovl}}$  in both loading and unloading phase) and  $\underline{U}^{F_{\min}}$  the dis-  
 119 placement field at  $F_{\min}$ .

120 The variation of the vertical component of the displacement vector field is depicted  
 121 for 4 cycles with overload at  $F_{\text{ovl}}$  and the cycle right before each overload at  $F_{\text{max}}$   
 122 (Table 3). For every overload, the displacement magnitude increases in comparison  
 123 to the precedent cycle, this increase is expected because the load is proportional  
 124 to displacement magnitude. A projection onto Williams' series expansion was then  
 125 performed using these displacement fields, leading to the extraction of crack features.

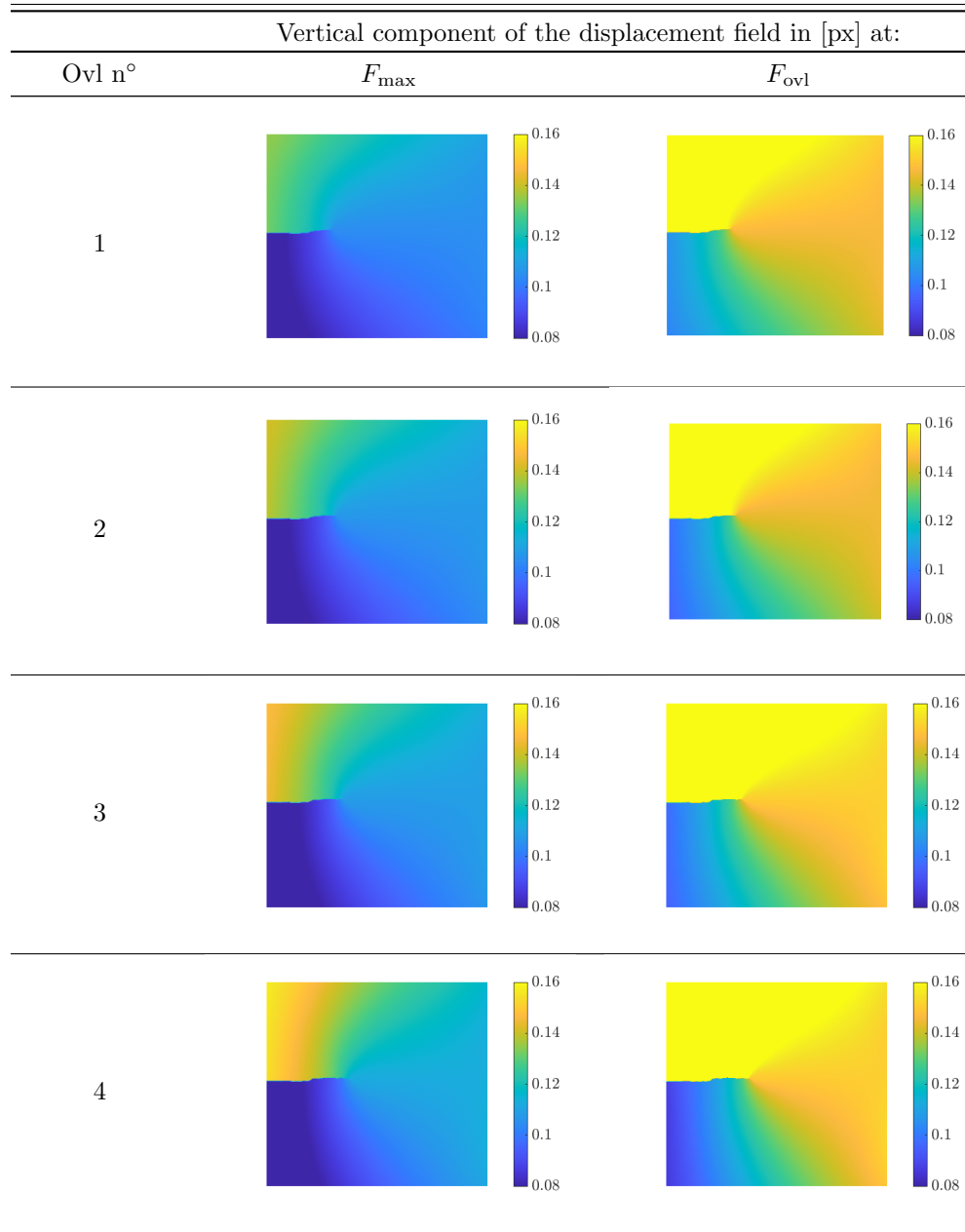
## 126 2.3 Asymptotic displacement using Williams' series

Williams [21] provides the asymptotic representation of the displacement field near a crack tip in linear elastic isotropic materials. The power of Williams series expansion is the preminent asymptotic description of the displacement fields near a crack tip in the conventional LFEM.

The 2D displacement field is expressed in the polar coordinate system crack tip centered as follows (Figure 5):

$$\delta_t \underline{U}_W(r, \theta) = \sum_{n=-\infty}^{+\infty} \delta_t a_I^n \underline{\phi}_I^n(\theta) r^{\frac{n}{2}}, \quad (2)$$

**Table 3** Vertical component of the displacement field in [px] at  $F_{\max}$  (left) and  $F_{\text{ovl}}$  (right) for cycles with overload and their precedent respectively.





127 with  $\delta_t a_I^n$  Williams' coefficients and  $\phi$  a base function.  $\underline{\phi}_I^n(\theta)$  is expressed in a complex  
 128 basis with  $i$  the complex number as follows:

$$\underline{\phi}_I^n = \frac{1}{\mu\sqrt{8\pi}} \left[ \kappa e^{in\theta/2} - \frac{n}{2} e^{i(4-n)\theta/2} + \left( \frac{n}{2} + (-1)^n \right) e^{-i(4-n)\theta/2} \right], \quad (3)$$

129 with  $\mu=28.46$  GPa and  $\kappa=2.07$  the shear modulus and Kolosov's constant respec-  
 130 tively.  $\nu=0.3$  is the Poisson's ratio.  
 131 Negative values of  $n$  are typically disregarded because they would lead to an infinite  
 132 strain energy density at the crack tip. However, the crack tip position being unknown,  
 133 the first supersingular term ( $n = -1$ ) is used to estimate the position to the equiv-  
 134 alent elastic crack tip along a pre-defined crack path [3]. In the vicinity of the crack  
 135 tip,  $n = 0$  refers to the rigid body translations,  $n = 1$  ( $\delta K_I$ ) to singular stress,  $n = 2$   
 136 ( $\delta T$ ) to the uniform stress and  $n = 3$  ( $\delta B$ ) to the third term in the Williams series.

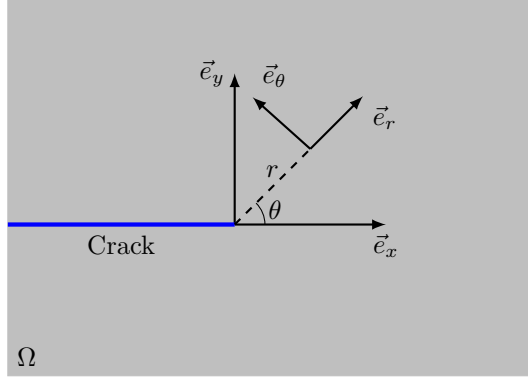


**Fig. 5:** Cartesian and cylindrical coordinate system around the crack tip in a solid  $\Omega$ .

## 137 2.4 Crack features extraction

In order to convert the DIC displacement fields in the dictionary of LEFM defined by the Williams' series, a projection (in the least squares sense) of  $\delta \underline{U}$  onto the analytical expression was performed and different fracture mechanics features was derived (e.g.  $\delta_t K_I$ ,  $\delta_t T$ ,  $\delta_t B$  and crack tip position)[9, 8, 10]. The following objective function (eq. 4) was minimized:

$$\delta_t a_I^n = \arg \min_{\delta_t a_I^n} \{ \|\delta \underline{U}_{\text{DIC}} - \delta \underline{U}_{\text{W}}(\delta_t a_I^n)\|_2 \} \quad (4)$$

138 where  $\|\delta \underline{U}_{\text{DIC}} - \delta \underline{U}_{\text{W}}\|_2$  refers to the norm over all the nodes.

139 The projection domain, as illustrated in Figure 6, is an annulus characterized by its  
 140 external and internal radii, denoted as  $r_{\text{ext}}=2.4$  mm and  $r_{\text{int}}=0.29$  mm. A region above  
 141 and below the crack faces of  $r_{\text{int}}$  width is also excluded as the FE DIC does not describe

142 explicitly the displacement discontinuity. The internal radius  $r_{\text{int}}$  was considered to  
 143 exclude the close vicinity of the crack tip where DIC may be less reliable and because  
 144 the use of supersingular terms would lead to an ill-conditioned projection matrix. The  
 145 external radius  $r_{\text{ext}}$  has to be small enough to avoid influences of the free boundaries,  
 146 but large enough to include sufficient mesh points in the domain. The right size of the  
 147 projection domain, i.e. defining  $r_{\text{ext}}$  and  $r_{\text{int}}$ , has been identified through a parametric  
 148 study ensuring that the values of crack features are not sensitive to the size of the  
 149 projection domain.

150 Equation 2 affirms, that displacements can be computed for an infinite sum of modes.  
 151 However, limiting the solution from  $n_{\text{min}} = -3$  to  $n_{\text{max}} = 7$  is sufficient to retain the  
 152 relevant crack parameters [4].

153 Thus, the displacement field in mode I around the crack tip can be written as follows:

$$\begin{aligned}
 \delta_t \underline{U}_W &= \sum_{n_{\text{min}}}^{-1} \underbrace{\delta_t a_I^n \underline{\phi}_I^n(\theta) r^{\frac{n}{2}}}_{\text{supersingular terms}} + \underbrace{\delta_t a_I^0 \underline{\phi}_I^0(\theta)}_{\text{translation}} \\
 &+ \underbrace{\delta_t a_I^1 \underline{\phi}_I^1(\theta) \sqrt{r}}_{\text{singular term}} + \sum_2^{n_{\text{max}}} \underbrace{\delta_t a_I^n \underline{\phi}_I^n(\theta) r^{\frac{n}{2}}}_{\text{subsingular terms}} \\
 &= \sum_{n_{\text{min}}}^{-1} \underbrace{\delta_t a_I^n \underline{\phi}_I^n(\theta) r^{\frac{n}{2}}}_{\text{supersingular terms}} + \underbrace{\delta_t a_I^0 \underline{\phi}_I^0(\theta)}_{\text{translation}} \\
 &+ \underbrace{\delta_t K_I \underline{\phi}_I^1(\theta) \sqrt{r}}_{\text{singular term}} \\
 &+ \underbrace{\delta_t T \underline{\phi}_I^2(\theta) r + \delta_t B \underline{\phi}_I^3(\theta) / \sqrt{r} + \sum_4^{n_{\text{max}}} \delta_t a_I^n \underline{\phi}_I^n(\theta) r^{\frac{n}{2}}}_{\text{subsingular terms}} \tag{5}
 \end{aligned}$$

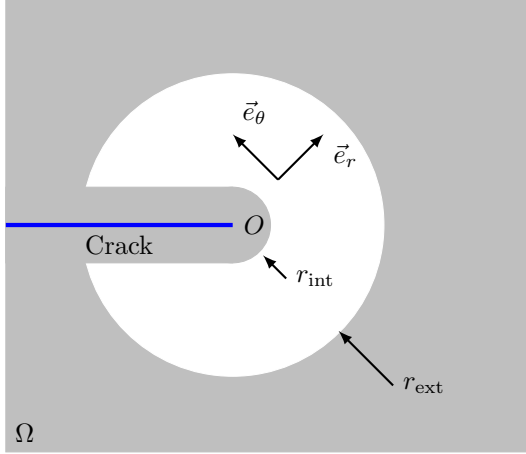


**Fig. 6:** Projection domain defined by  $r_{\text{ext}}$  the external radius and  $r_{\text{int}}$  the internal radius

### 154 3 Results

#### 155 3.1 Residual displacement analysis

156 An examination of the projection quality is necessary to validate the features  
 157 extraction. Thus we propose the following indicator:

$$\alpha = \frac{\|\delta \underline{U}_{\text{DIC}} - \delta \underline{U}_{\text{W}}\|_2}{N_{\text{nodes}}} \times \frac{\Delta F}{\delta_t F},$$

158 with  $\Delta F = F_{\text{max}} - F_{\text{min}}$ .

159  $\alpha$  is a measure of the normalized average nodal residual displacement amplitude. It is  
 160 scaled by  $\frac{\Delta F}{\delta_t F}$  to account for the increase of the displacement magnitude with the load  
 161  $\delta_t F$ . It is therefore, a good candidate to quantify the quality of features extraction  
 162 and displacement field reconstruction.

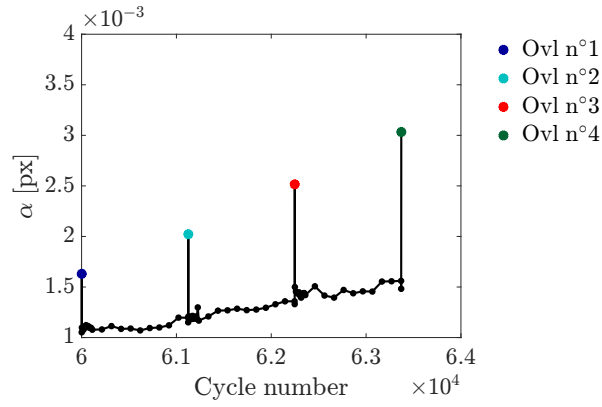


**Fig. 7:** Normalized average nodal residual displacement amplitude  $\alpha$  as a function of the number of cycles

163 Figure 7 shows  $\alpha$  as a function of the number of cycles during the loading phase, 4  
 164 peaks corresponding to 4 overloads are seen. The figure depicts an upward tendency.  
 165 Due to the crack propagation, the displacement magnitude increase and thus  $\alpha$   
 166 also. However the values are below 0.01 pixel which, in view of displacement values  
 167 observed in Table 3, means that the reconstruction of the displacement fields from  
 168 Williams' series was very accurate.

169

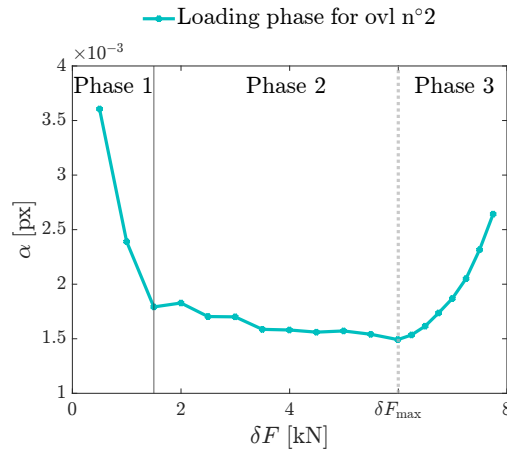


**Fig. 8:** Example of a normalized average nodal displacement error amplitude  $\alpha$  as a function of the load for the second overload in the loading phase

170 Figure 8 depicts  $\alpha$  as a function of the load during the loading phase of a cycle with  
 171 overload. Here three phases are seen. Phase 1 shows a significant decrease in  $\alpha$ , which

172 can be explained by the fact that  $\delta F$  growth from zero while the measured displace-  
173 ment growth from a small but finite value. In Phase 2, we observe a plateau, indicating  
174 that the average extraction residual is proportional to the displacement magnitude  
175 (or equivalently the applied load). Finally, in Phase 3, which is the overloading phase,  
176 we notice an increase in  $\alpha$  and it is probably due to the significant displacement mag-  
177 nitudes or again partly because Williams' series are less appropriate to reconstruct  
178 the displacement during overload. However, all values remain below 0.01 pixel which  
179 means that the features are successfully extracted even in the overloading phase.

### 180 **3.2 Crack features**

181 Here, we choose to present 3 crack features ( $\delta K_I$ ,  $\delta T$  and  $\delta B$ ), the 4 others are  
182 presented in the Appendix section in Figure A1. These features are presented in the  
183 following plots (Figure 9 and Figure 10) depicting their evolution upon  $\delta F$  for 4 cycles  
184 with overload and the cycle just before each overload. For these plots, continuous  
185 lines are used for the loading phase while dashed lines denotes the unloading phase.  
186

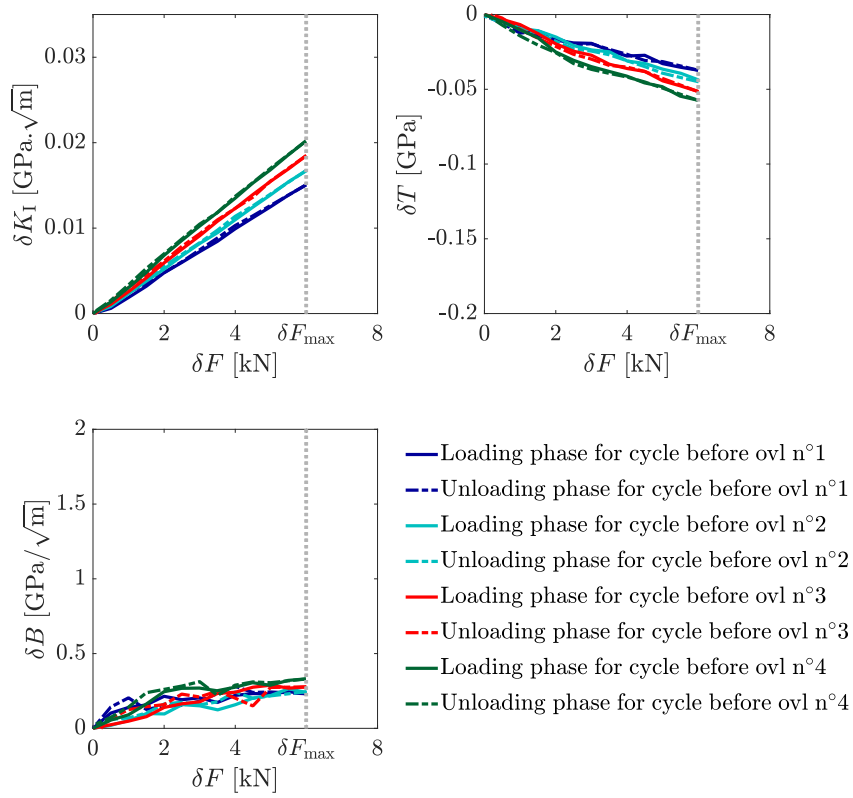


**Fig. 9:** Crack features ( $\delta K_I$ ,  $\delta T$  and  $\delta B$ ) as a function of the  $\delta F$  for the cycle right before each overload

187 Figure 9 shows the features as a function of the load. The same behavior can be  
 188 seen for all features, they exhibit a single regime where they are all proportional to  $\delta F$   
 189 both during loading and unloading phase. The slope value of these features increase  
 190 from an overload to the other, reflecting the growing displacement magnitude caused  
 191 by crack propagation.  $\delta B$  is less smooth than  $\delta K_I$  and  $\delta T$ . These observations are  
 192 consistent with LEFM assumptions.

193

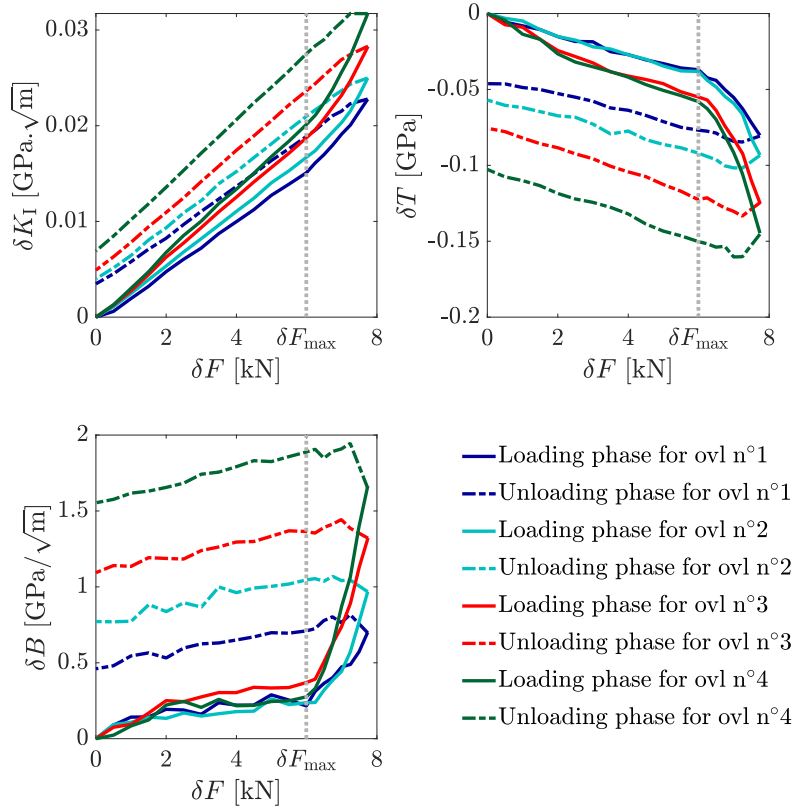


**Fig. 10:** Crack features ( $\delta K_I$ ,  $\delta T$  and  $\delta B$ ) as a function of  $\delta F$  for cycles with overload

194 Figure 10 shows crack features as a function of the load  $\delta F$  during cycles with  
 195 overload. The same behavior is observed for the three features. The loading phase  
 196 (from  $F_{\min}$  to  $F_{\max}$ ) shows a proportional regime to  $\delta F$ . This regime changes during  
 197 the overloading phase (from  $F_{\max}$  to  $F_{ovl}$ ), here crack features increase faster than  
 198  $\delta F$  making this growth an overload signature. The unloading phase is linear with  $\delta F$ ,  
 199 it apparently maintains the same slope as observed during the loading phase.  
 200

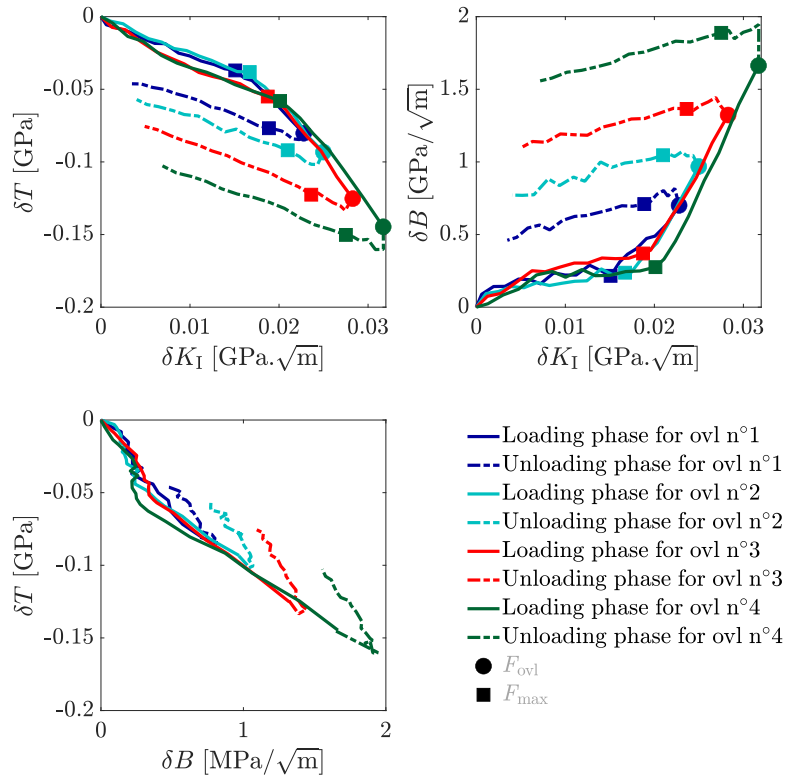


**Fig. 11:**  $(\delta K_I, \delta T)$  ,  $(\delta K_I, \delta B)$  and  $(\delta B, \delta T)$  plots for cycles with overload

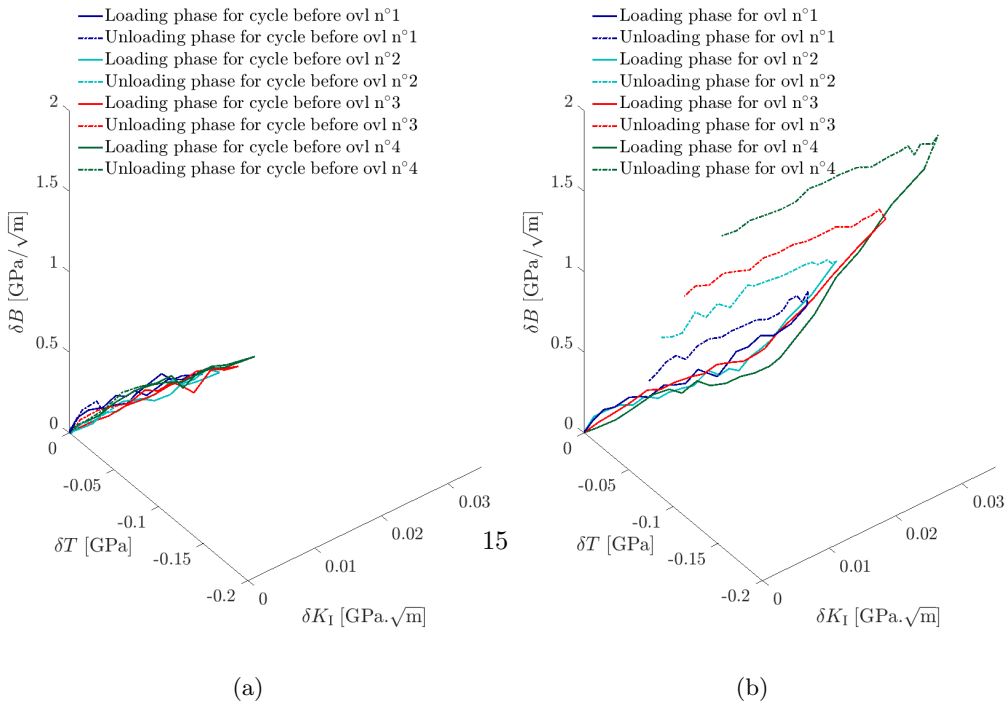


**Fig. 12:** 3D representation of  $\delta K_I$  ,  $\delta T$  and  $\delta B$  for cycles before overload (a) and during overload (b)



201 Figure 11 shows  $\delta T$  as a function of  $\delta K_I$  and  $\delta B$  as a function of  $\delta K_I$ , during the  
 202 loading phase  $\delta T$  and  $\delta B$  depicts respectively a proportional regime to  $\delta K_I$ , then this  
 203 regime changes during the overloading phase where  $\delta T$  and  $\delta B$  grows faster than  $\delta K_I$ .  
 204 The unloading phase maintains almost the same slope as observed during the loading  
 205 phase. The two hysteresis shows that in a case of a cycle with overload  $\delta T$  and  $\delta B$  are  
 206 not proportional to  $\delta K_I$ .

207 The third plot shows  $\delta T$  against  $\delta B$ , a strong correlation is observed between the two  
 208 features. These three plots suggests that  $\delta K_I$  is an independent feature, while  $\delta T$  and  
 209  $\delta B$  are dependent on each other.

210 To better understand the link, Figure 12 shows the crack features state representation  
 211 in the  $(\delta K_I, \delta T, \delta B)$  space during a cycle without overload (a) and with overload (b).  
 212 In a case without overload a clear line is observed, signifying, as observed previously,  
 213 that all the crack features are proportional to each other. In a case with overload the  
 214 crack features coordinates seem to lie in a plane. In these two distinct cases, quali-  
 215 tatively different structures are observed. In the next section, we will analyze these  
 216 geometries and propose an appropriate basis to describe each of them.

217 All the data presented above are available in the following doi: 10.5281/zen-  
 218 do.10795209 .

## 219 4 Analysis

### 220 4.1 Singular Value Decomposition

As strong correlations are observed among the previously identified features, we propose an analysis based on the Singular Value Decomposition (SVD) to further reduce the number of relevant features. The SVD is carried out on a rectangular matrix  $A_{ft}$  that gathers for a single cycle all the features at all time steps. The line index  $f$  corresponds to the singular and subsingular coefficients in Williams' series expansion  $\delta_t a_I^f$  with  $f$  ranging from  $f = 1$  to  $f = 7$ . The column index  $t$  corresponds to the loading steps with  $t$  ranging from  $t = 1$  to  $t = 26$  in a case without overload and  $t = 38$  otherwise. The rank of the matrix  $A_{ft}$  is therefore at most 7. Additionally, each line of  $A_{ft}$  is rescaled to make it dimensionless:

$$A_{ft} = \delta_t a_I^f \cdot \frac{r_c^{\frac{f}{2}-1}}{E}, \quad (6)$$

221 where  $r_c = r_{\max}$  is a characteristic length and  $E$  is the Young's modulus.

The SVD of  $A_{ft}$  can be written as follows:

$$A_{ft} = \sum_{i=1}^{\text{rank}(A_{ft})} U_f^{(i)} \sigma^{(i)} V_t^{(i)}, \quad (7)$$

222 with

223 •  $\sum_f U_f^{(i)} \cdot U_f^{(j)} = \delta_{ij}$  and  $U_f^{(i)}$  is the  $i^{\text{th}}$  left singular vector,

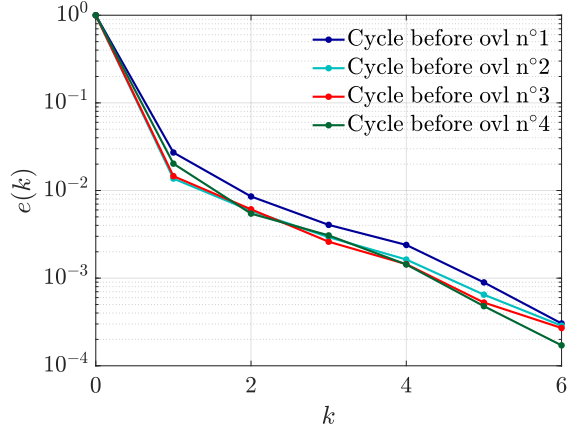
- 224 •  $\sigma^{(i)} \geq \sigma^{(j)}$  for  $i < j$  and  $\sigma^{(i)}$  is the  $i^{th}$  singular value,
- 225 •  $\sum_t V_t^{(i)} \cdot V_t^{(j)} = \delta_{ij}$  and  $V_t^{(i)}$  is the  $i^{th}$  right singular vector.

Before analyzing the decomposition, the reconstruction error is computed. From the SVD it is indeed possible to compute  $\tilde{A}_{ft}^k$ , the best rank- $k$  approximation of  $A_{ft}$  as:

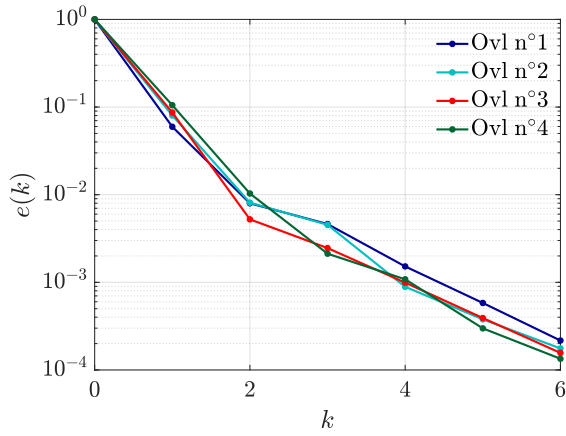
$$\tilde{A}_{ft}^k = \sum_{i=1}^k U_f^{(i)} \sigma^{(i)} V_t^{(i)}, \quad (8)$$

with  $k \leq \text{rank}(A_{ft})$ . The relative approximation error in Fröbenius norm, ranging from 0 ( $k=\text{rank}(A_{ft})$ ) to 1 ( $k=0$ ), writes:

$$e(k) = \frac{\|A_{ft} - \tilde{A}_{ft}^k\|_F}{\|A_{ft}\|_F} = \frac{\sqrt{\sum_{i=k+1}^{\text{rank}(A_{ft})} \sigma^{(i)^2}}}{\sqrt{\sum_{i=1}^{\text{rank}(A_{ft})} \sigma^{(i)^2}}}. \quad (9)$$



(a) Cycles without overload



(b) Cycles with overload

**Fig. 13:** Relative approximation error versus the number of terms  $k$

Figure 13 shows the relative approximation error as a function of  $k$ . For cycles without overload, the relative error drops below 1% with just a single term. Adding more terms has a limited effect as illustrated by the slope reduction beyond  $k = 1$ . This suggests that a single term is adequate for accurately describing the matrix  $A_{ft}$  in a cycle without overload. This was expected because the crack features are proportional to each other as seen in Figure 12 (a). For cycles with overload, two terms are needed to reach approximately a relative error of 1%. This corresponds also to a slope change in the reconstruction error which means that an additional descriptor is needed compared to the previous case. This confirms and generalizes the observation made in

Figure 12 (b): all the points which co-ordinates in the space of the  $\delta_t a_I^f$  Williams' coefficients are defined in  $A_{ft}$  approximately lie on a plane generated by the orthogonal basis  $(U_f^{(1)}, U_f^{(2)})$ . To validate this approximation, we defined, in Equations (10,11,12),  $\delta_t \tilde{K}_I, \delta_t \tilde{T}$  and  $\delta_t \tilde{B}$  the SVD reconstruction of the crack features as follows:

$$\delta_t \tilde{K}_I = \tilde{A}_{1t}^{(2)} \cdot \frac{E}{r_c^{\frac{-1}{2}}} \quad (10)$$

$$\delta_t \tilde{T}(t) = \tilde{A}_{2t}^{(2)} \cdot E \quad (11)$$

$$\delta_t \tilde{B}(t) = \tilde{A}_{3t}^{(2)} \cdot \frac{E}{r_c^{\frac{1}{2}}} \quad (12)$$

226 A comparison with the original crack features is shown in Figure 14. Other crack  
227 features (from  $n = 4$  to  $n = 7$ ) are shown in the appendix section in Figure A1.

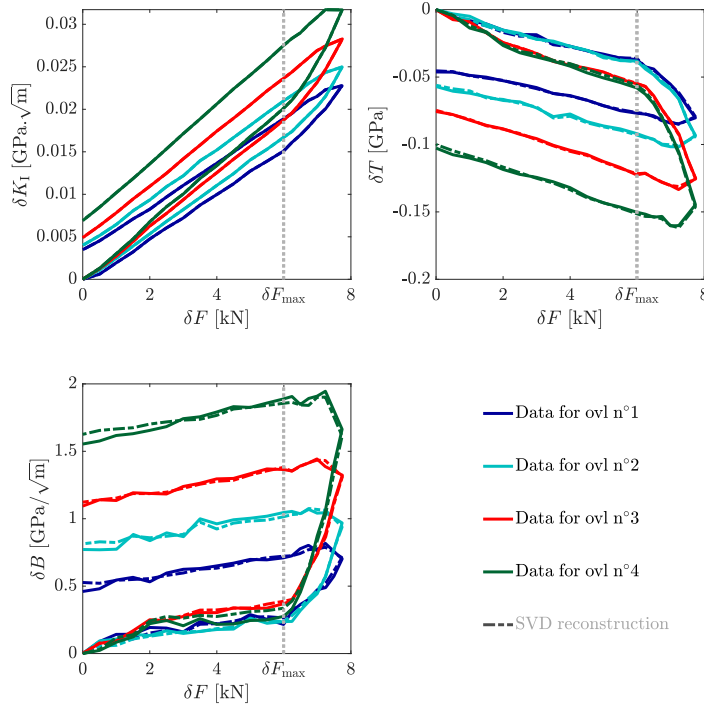


**Fig. 14:** Crack features ( $\delta K_I$ ,  $\delta T$  and  $\delta B$ ) and their SVD reconstruction ( $\delta \tilde{K}_I$ ,  $\delta \tilde{T}$  and  $\delta \tilde{B}$ ) as a function of  $\delta F$  for cycles with overload

228 We can clearly see that the SVD reconstruction of the crack features is accurate.  
 229 For  $\delta K_I$ , it is difficult to distinguish between the reconstructed data and the original  
 230 data. Tiny differences exist for  $\delta T$ . Finally, the rank 2 reconstruction smoothes  $\delta B$  for  
 231  $\delta F \leq \delta F_{\max}$ .

232 For the cycles without overload, the evolution of the crack tip state is obviously  
 233 dominated by  $\delta K_I$ . Its contribution  $U_1^{(1)}$  to the single mode required for a robust  
 234 reconstruction of the crack feature evolution is around 99%. Analyzing the results of  
 235 the SVD for the cycles with overload allows to obtain the two linear combinations of  
 236 the original crack features describing the evolution of the crack tip state in the most  
 237 condensed but robust way (as shown by the low reconstruction errors). As illustrated  
 238 in Figure 15, the first mode defined by  $U_f^{(1)}$  is similar for all the overload cycles and is  
 239 dominated by the contribution of  $\delta K_I$  ( $f = 1$ ) but still contains some contribution of  
 240  $\delta T$  ( $f = 2$ ) and  $\delta B$  ( $f = 3$ ). Concerning the second left singular vector  $U_f^{(2)}$ , the main  
 241 contribution comes from the second and third crack features, namely  $\delta T$  and  $\delta B$ .

242 This change in the number of required left singular vectors when analyzing cycles  
 243 without overload and cycles with overload and their coordinates in the crack features  
 244 space, unquestionably suggests that  $\delta K_I$  cannot be considered as the unique descriptor  
 245 of the kinematic field around the crack tip when an overload is applied. This also  
 246 suggests that additional sub-singular terms must be included to properly describe the  
 247 crack tip kinematic field.

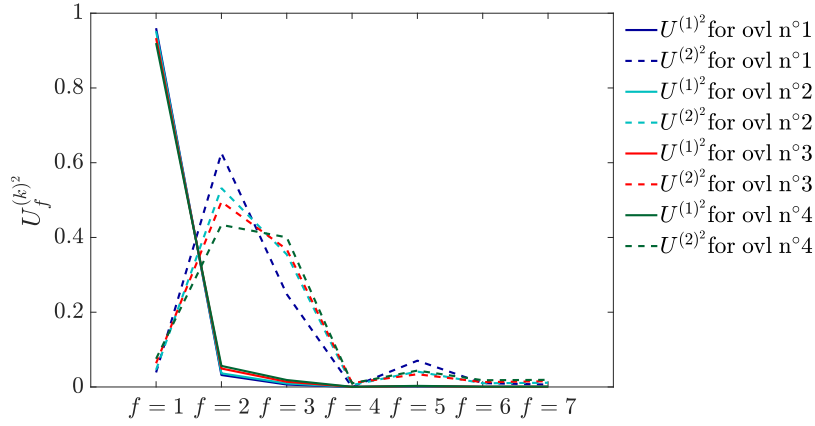
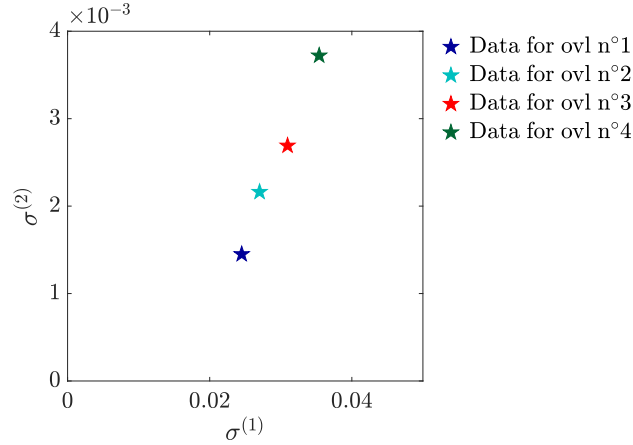


Fig. 15:  $U_f^{(k)2}$  for  $k = 1$  and  $k = 2$  for all cycles with overload

## 248 4.2 Evolution of the crack tip state

249 An other interesting point is that, from Figure 16, the amplitude of the second singular  
 250 value  $\sigma^{(2)}$  grows faster, between overloads, than the amplitude of the first singular  
 251 value  $\sigma^{(1)}$ . This suggests that the increase in crack length induces an increase in the  
 252 contribution of the second singular value compared to the first one.



**Fig. 16:**  $\sigma^{(2)}$  as a function  $\sigma^{(1)}$  for all cycles with overload

253 Let us remind that the two vectors  $(U_f^{(1)}, U_f^{(2)})$  actually define a basis of the  
 254 best approximating plane, in the 7 dimensional space of the crack features, to the  
 255 data contained in  $A_{ft}$ . Figure 12 clearly illustrates the existence of this plane in  
 256 the  $(\delta K_I, \delta T, \delta B)$  space. The strong, but not perfect correlation between  $\delta T$  and  $\delta B$   
 257 observed in Figure 11 suggested that the normal to this plane is not in the  $(\delta T, \delta B)$   
 258 plane. This is confirmed by the analysis of the two dominant left singular vectors  
 259 of the SVD  $U_f^{(1)}$  and  $U_f^{(2)}$  which both contain a non-vanishing contribution of  $\delta K_I$   
 260 ( $f = 1$ ). The evolution of the crack tip state in terms of the two dominant left sin-  
 261 gular vectors is now analysed in this plane. For this purpose, the trajectories in the  
 262  $(U_f^{(1)}, U_f^{(2)})$  plane, defined by  $(\sigma^{(1)}V_t^{(1)}, \sigma^{(2)}V_t^{(2)})$  are plotted in Figure 17. It is clearly  
 263 observed that the trajectories are similar up to a scaling respectively defined by  $\sigma^{(1)}$   
 264 and  $\sigma^{(2)}$  along the two directions. As the crack propagates from the first overload to  
 265 the fourth one, we observe that  $\sigma^{(1)}$  and  $\sigma^{(2)}$  increase at different rates (see Figure 16)  
 266 making this change in the trajectories not a pure dilation. To further confirm that the  
 267 crack tip loading paths, once represented in the plane defined by the two dominant  
 268 left singular vectors  $U_f^{(1)}$  and  $U_f^{(2)}$ , is of the same nature, the trajectories defined by  
 269  $(V_t^{(1)}, V_t^{(2)})$  are plotted in Figure 18. With this representation of the data, it is clear  
 270 that the crack tip loading path (the evolution of the crack features with respect to  
 271  $\delta F$ ) is the same irrespective of the crack length. Indeed, as a master curve emerges  
 272 from  $(V_t^{(1)}, V_t^{(2)})$ , we confirm the unique nature of the crack features evolution when  
 273 it is presented in the appropriate space. The crack tip loading path is defined by two  
 274 parallel linear branches for  $\delta F \leq \delta F_{\max}$  and a third smooth branch joining the first  
 275 two ones during the overloading phase.

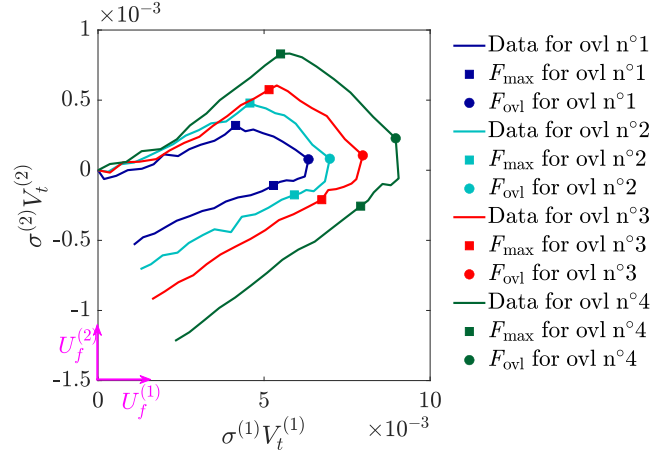


**Fig. 17:**  $\sigma^{(2)}V_t^{(2)}$  as a function  $\sigma^{(1)}V_t^{(1)}$  for all cycles with overload expressed in the  $(U_f^{(1)}, U_f^{(2)})$  basis

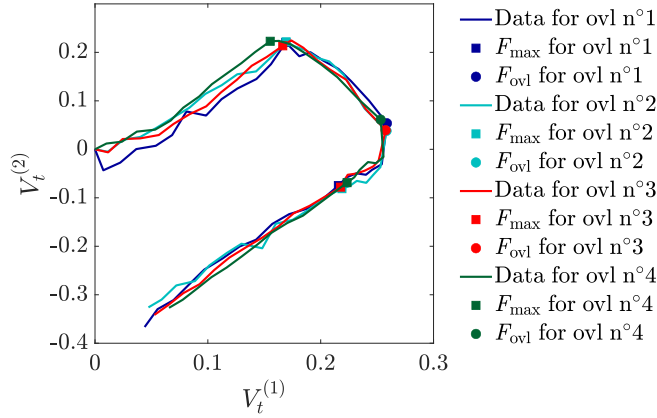


**Fig. 18:**  $V_t^{(2)}$  as a function  $V_t^{(1)}$  for all cycles with overload

## 276 5 Discussion: towards a constitutive description of 277 crack tip states

278 From the crack features evolution during cycles with and without overload presented  
279 in Section 3, the use of a SVD allows us to extract the main characteristics of the  
280 evolution of the kinematic field around the crack tip. For the cycles without overload,  
281 it is confirmed that considering a single descriptor, that can be considered to be  $\delta K_I$ ,

282 is enough. Conversely, non-singular terms must be considered when an overload is  
 283 applied. Two linear combinations ( $U_f^{(1)}, U_f^{(2)}$ ) of crack features (vectors in the crack  
 284 features space) must actually be considered in this case. If the crack tip loading path  
 285 is considered in the plane defined by these two vectors a non-proportional loading  
 286 (trajectories in ( $V_t^{(1)}, V_t^{(2)}$ ) plotted in Figure 18) is obtained. The intensities of the  
 287 loading along these two elementary path descriptors are however different when their  
 288 evolution with the crack length is considered (see Figure 16).

289 In the proposed analysis, the SVD is performed independently for each loading  
 290 cycle. As observed in Figure 15, the coordinates of ( $U_f^{(1)}, U_f^{(2)}$ ) in the crack features  
 291 space are slightly changed from one overload to the next one. Thus, while the interpre-  
 292 tation in terms of loading paths defined by the two dominant modes (see trajectories  
 293 in ( $V_t^{(1)}, V_t^{(2)}$ ) is unquestionable, the contribution of these 2 modes once translated  
 294 into a displacement basis (thanks to the original Williams' functions ) is not that  
 295 straightforward. Part of these changes in ( $U_f^{(1)}, U_f^{(2)}$ ) can be attributed to the increase  
 296 of the crack length, the dependency of  $\delta K_I/\delta F$ ,  $\delta T/\delta F$  and  $\delta B/\delta F$  and all the other  
 297 crack features per unit load with respect to the crack length being different and depen-  
 298 dent on the specimen geometry. Also, as illustrated in Figure 19, the evolution of  
 299 the contribution of the two right singular vectors ( $V_t^{(1)}, V_t^{(2)}$ ) with the applied load  
 300  $\delta F$  is non-linear. This means that the non-linear evolution of the crack features with  
 301  $\delta F$ , see Figure 11, is reported on the two dominant left singular vectors ( $U_f^{(1)}, U_f^{(2)}$ ).  
 302 With this respect, the interpretation of the respective contribution of  $U_f^{(1)}$  and  $U_f^{(2)}$   
 303 is difficult. In particular it is not possible at that point to separate the displacement  
 304 around the crack in a mode evolving linearly with  $\delta F$  (expected to be the same as for  
 305 the case without overload and to be dependent only on the crack length) and another  
 306 one holding the non-linear dependence on  $\delta F$ . It also makes difficult to interpret the  
 307 different evolution of the singular values  $\sigma^{(1)}$  and  $\sigma^{(2)}$  illustrated in Figure 16.

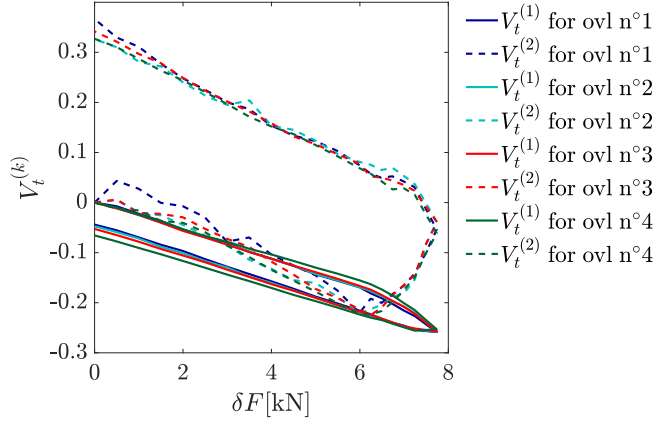


**Fig. 19:**  $V_t^{(k)}$  as a function of  $\delta F$  for all cycles with overload



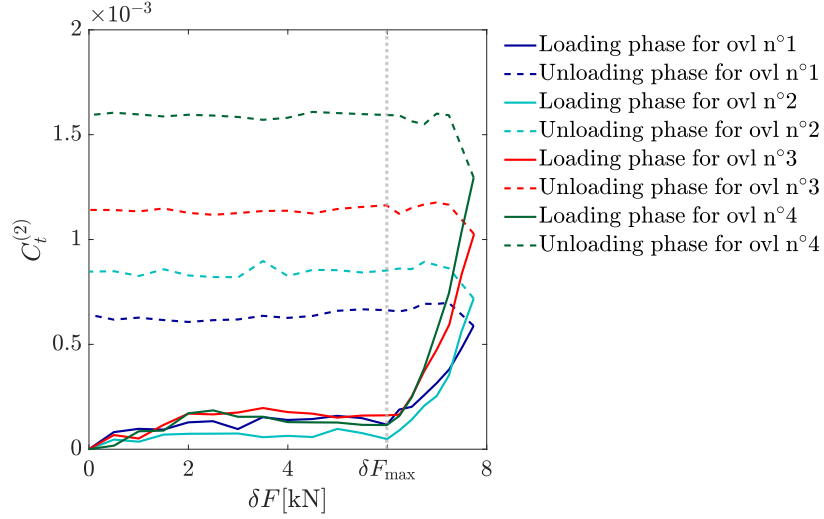


**Fig. 20:**  $C^{(2)}$  as a function  $\delta F$  for all cycles with overload

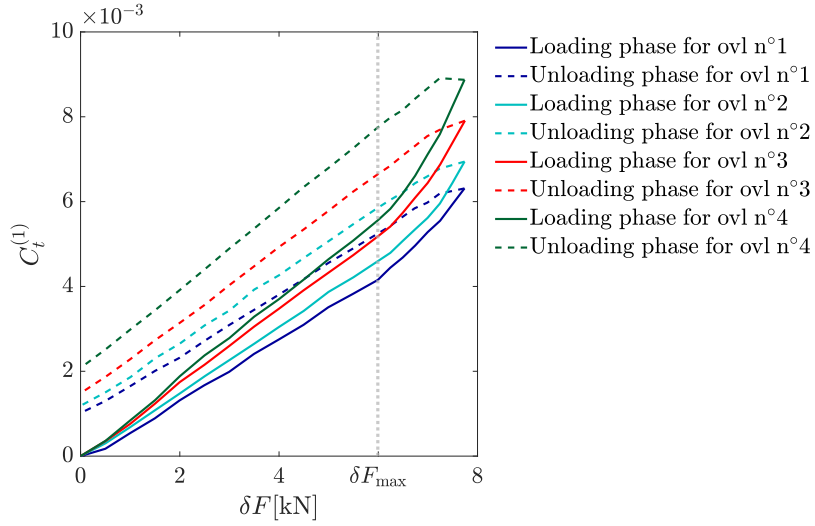


**Fig. 21:**  $C^{(1)}$  as a function  $\delta F$  for all cycles with overload

308 As a first attempt to improve the level of comprehension, we propose to recombine  
 309 the two modes  $(U_f^{(1)}, U_f^{(2)})$  into  $(\tilde{U}_f^{(1)}, \tilde{U}_f^{(2)})$  so that when  $\delta F \leq \delta F_{\max}$  the contribution  
 310 of  $\tilde{U}_f^{(2)}$  remains constant. In other words, the sought recombination of the two modes  
 311 should allow to align the linear branches of the trajectories in Figure 17 and Figure 18

312 with the horizontal axis. This recombination simply consists in a rotation of the ini-  
 313 tial orthogonal basis  $(U_f^{(1)}, U_f^{(2)})$  within the plane where the data lies on in the crack  
 314 features space. This rotation is obtained by computing a new SVD on a rectangular  
 315 matrix containing  $\sigma^{(1)}V_t^{(1)}, \sigma^{(2)}V_t^{(2)}$  during the unloading phase (the linear branch  
 316 corresponding to the unloading phase from  $\delta F_{\max}$  to 0) as two lines of a rectangular  
 317 matrix. The two left singular vectors (having two components) are then combined in  
 318 a  $2 \times 2$  matrix allowing for rotating from the initial singular vector basis  $(U_f^{(1)}, U_f^{(2)})$   
 319 into a new basis  $(\tilde{U}_f^{(1)}, \tilde{U}_f^{(2)})$ . The evolution of the contribution of these two modified  
 320 modes is contained into two vectors  $C_t^{(1)}, C_t^{(2)}$  resulting from the rotation of  $\sigma^{(1)}V_t^{(1)},$   
 321  $\sigma^{(2)}V_t^{(2)}$ . Figure 20 shows  $C_t^{(2)}$  as a function of  $\delta F$ . It is clearly observed that when  
 322  $\delta F \leq \delta F_{\max}$ ,  $C_t^{(2)}$  remains constant and that a non-linear increases of its amplitude  
 323 is obtained during the overloading phase of the cycles. This behaviour is as expected  
 324 and can be interpreted more clearly. This second mode is now only activated in the  
 325 overloading part of the cycles when  $\delta F \geq \delta F_{\max}$ . However, Figure 21 shows that  
 326 the first mode that was expected to depend linearly on  $\delta F$  still evolves non-linearly  
 327 with respect to  $\delta F$ . Graphically, this can be explained by examining Figure 18. As  
 328 mentioned earlier, the loading paths in this graph consist in two linear branches for  
 329  $\delta F \leq \delta F_{\max}$  connected by a curved branch corresponding to the overload phase of the  
 330 cycle. Roughly speaking, the main orientation of this curved branch is not orthogonal  
 331 to the two parallel linear branches. However, the decompositions used so far lead  
 332 orthonormal basis vectors. This means that the projection of the curved branch  
 333 onto a vector oriented along the linear branches does not vanish. As a consequence  
 334 the contribution of the first modified mode  $\tilde{U}_f^{(1)}$  exhibits the non-linear evolution  
 335 observed in Figure 21. To further improve the analysis and to try and providing a  
 336 decomposition of the crack features into two composites features encoding the linear  
 337 and non-linear evolution of the kinematic field around the crack tip as a function  
 338 of the applied load, an alternative decomposition is suggested. Following the above  
 339 described graphical interpretation, the linear / non-linear decomposition should be  
 340 performed onto a non-orthogonal basis, the first basis vector being aligned with the  
 341 linear branches and the second one with the main orientation of the curved branch.  
 342

For this purpose, the left singular vector  $U_f^1$  further referred to as *linear* is defined  
 as  $\tilde{U}_f^{(1)}$ . Then, a linear prediction of  $A_{ft'}$  for  $t'$  the steps during the unloading phase  
 from  $\delta F_{\max}$  to 0 is built. This linear prediction is obtained through an amplitude  
 vector  $C_{t'}^1 \propto \delta F$  such that at  $\delta F = \delta F_{\max}$

$$U_f^1 C_{t'}^1 \approx A_{ft'}. \quad (13)$$

At this stage,  $C_{t'}^1$  is not aimed at reconstructing  $A_{ft'}$  accurately but only at giving  
 a linear prediction aligned with  $U_f^1$ . Then an other SVD is carried out on a residual  
 rectangular matrix  $A_{ft}^{res}$  defined as follows:

$$A_{ft}^{res} = A_{ft} - U_f^1 C_t^1. \quad (14)$$

343 The rank of  $A_{ft}^{\text{res}}$  can be expected to be the same as that of  $A_{ft}$ . However, because of  
 344 the particular shape of the  $(V_t^{(1)}, V_t^{(2)})$  trajectories with two parallel linear branches  
 345 and one curved (but almost linear) branch, and because a linear prediction  $U_f^1 C_t^1$  along  
 346 the orientation  $U_f^1$  of the parallel branches is subtracted from  $A_{ft}$ , only one mode is  
 347 required to accurately reconstruct  $A_{ft}^{\text{res}}$  as confirmed in Figure 22. The corresponding  
 348 left singular vector is set as  $U_f^{\text{nl}}$ . Processing the data as detailed above, one obtains  
 349 a non-orthogonal basis  $(U_f^1, U_f^{\text{nl}})$  of the plane previously defined by  $(U_f^{(1)}, U_f^{(2)})$  or  
 350 alternatively  $(\tilde{U}_f^{(1)}, \tilde{U}_f^{(2)})$ .

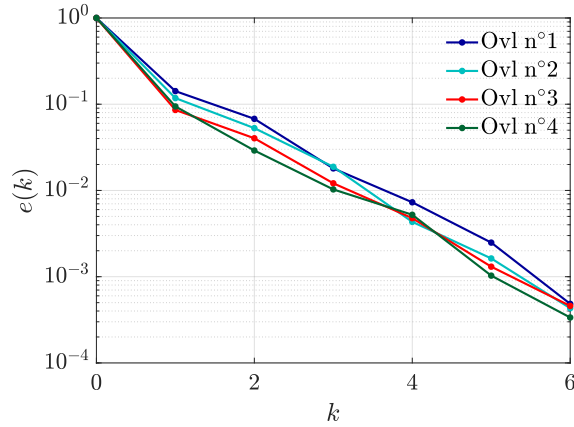


**Fig. 22:** Relative approximation error for  $A_{ft}^{\text{res}}$  reconstruction versus the number of terms  $k$

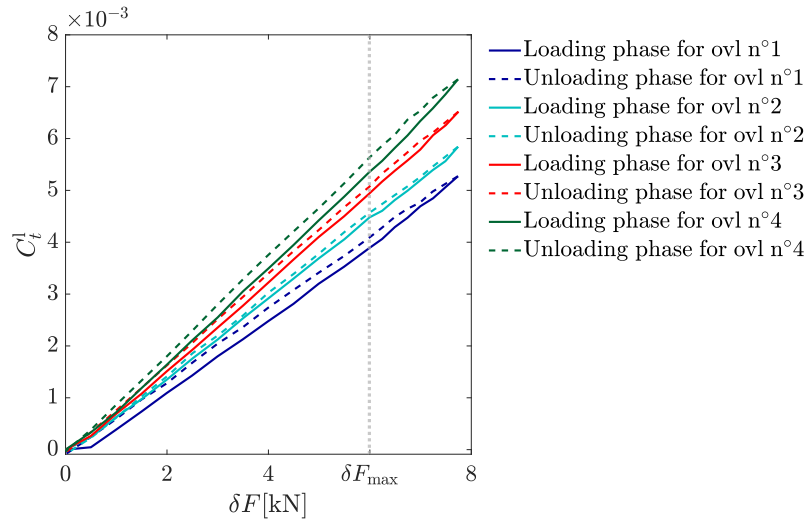


**Fig. 23:**  $C_t^1$  as a function of  $\delta F$  for all cycles with overload

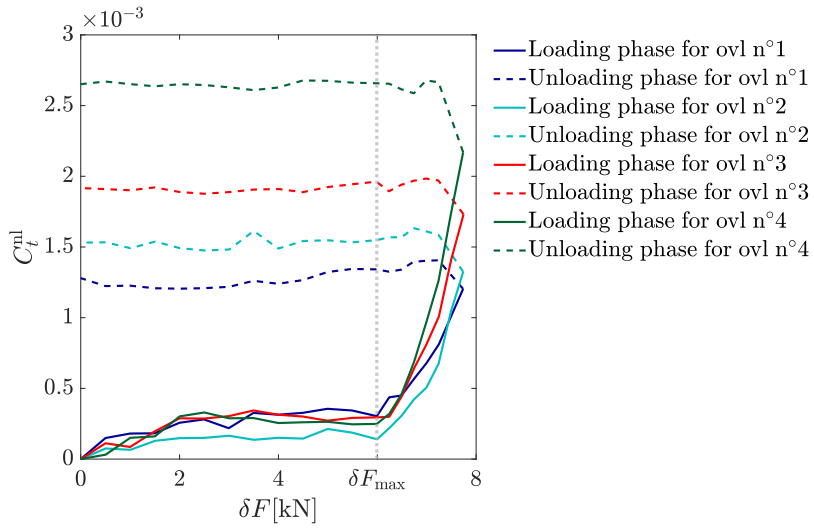


**Fig. 24:**  $C_t^{n1}$  as a function of  $\delta F$  for all cycles with overload

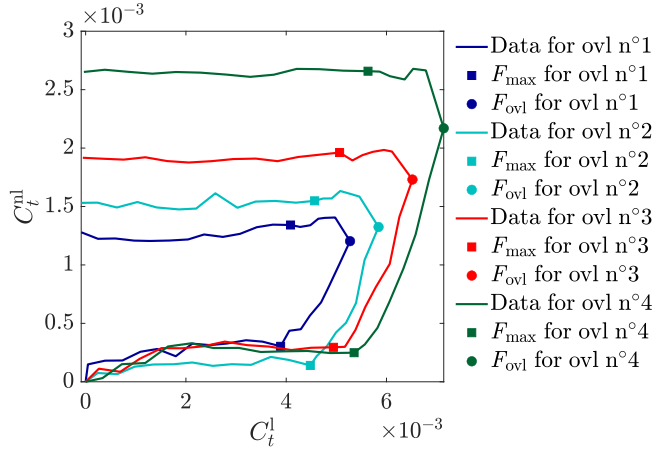


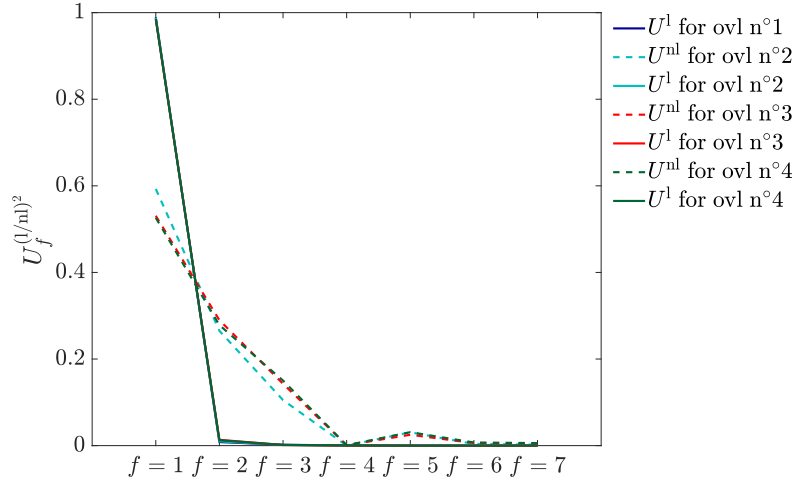
**Fig. 25:**  $C_t^{nl}$  as a function of  $C_t^l$  for all cycles with overload

351 Eventually, for any  $t$ ,  $A_{ft}$  is projected onto  $(U_f^l, U_f^{nl})$  leading to the definition  
 352 of  $C_t^l$  and  $C_t^{nl}$ . Defined as such,  $U_f^l C_t^l$ , respectively  $U_f^{nl} C_t^{nl}$ , encodes the linear (with  
 353 respect to  $\delta F$ ), respectively non-linear, evolution of  $A_{ft}$ . As illustrated in Figure 24,  
 354  $C_t^{nl}$  exhibits the same behavior as  $C_t^{(2)}$  in Figure 20 but as shown in Figure 23, the  
 355 complementary part encoded in  $U_f^l$  evolves linearly with respect to  $\delta F$ .

356 For a deeper understanding, Figure 26 shows the squared coordinates of  $(U_f^l$  and  
 357  $U_f^{nl})$  in the normalized crack features basis. Compared to previously obtained basis  
 358 (see Figure 15),  $U_f^l$  appears as almost perfectly aligned with the first crack feature  
 359 (*i.e.*  $\delta K_I$ ) while for the second vector  $U_f^{nl}$  the second and third features contribute  
 360 significantly. Note the contrary to what was presented in Figure 15, the first feature  
 361 has the highest amplitude for the second vector. Using these two vectors, Table 4,  
 362 respectively Table 5, shows the field reconstructed from Williams' basis functions and  
 363  $U_f^l, U_f^{nl}$  after rescaling (see Equation 6). As expected from Figure 26, the kinematic  
 364 fields corresponding to  $U_f^l$  are similar to that of the Williams' function for  $n = 1$ .  
 365 Those of  $U_f^{nl}$  behave differently, the main contribution comes from the three crack  
 366 features represented in the section 3.

367 Conceptually,  $U_f^l$  is sought to vary with the crack length and also to depend on  
 368 the specimen geometry. The amplitude  $C_t^l$  of its contribution of the kinematic field  
 369 is linear with respect to  $\delta F$ , this can be interpreted as the effect at the crack tip of  
 370 remote loading if the material behaves linearly.

371 Conversely,  $U_f^{nl}$  that is activated through  $C_t^{nl}$  encompasses the effect of the non-  
 372 linear constitutive behaviour of the material. It is expected that the constitutive  
 373 relation of the material affects not only the evolution of  $C_t^{nl}$  with respect to  $C_t^l$  which  
 374 can be interpreted as a flow rule (see Figure 25) but also the link between  $U_f^{nl}$  and  
 375  $U_f^l$  which one would be more prone to interpret as a yield criterion describing the  
 376 evolution of the yield surface upon the loading direction (here  $U_f^l$ ).

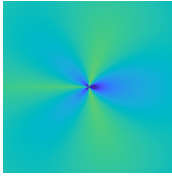
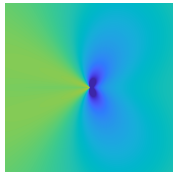
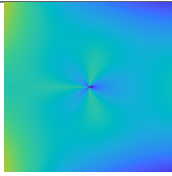
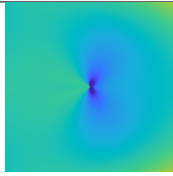


**Fig. 26:**  $U_f^l$  and  $U_f^{nl}$  for all cycles with overload

**Table 4** Displacement field corresponding to the linear and the non-linear modes of the SVD at  $F_{ovl}$  for the third overload.

Displacement field reconstruction		
mode	Horizontal component	Vertical component
Linear		
Non-linear		

**Table 5** Strain field corresponding to the linear and the non-linear modes of the SVD at  $F_{ovl}$  for the third overload.

Strain field reconstruction		
mode	$\epsilon_{xx}$	$\epsilon_{yy}$
Linear		
Non-linear		

## 6 Conclusion

377

378 In this paper, fatigue tests were conducted on a SENT specimen, pictures were taken  
 379 for DIC processing, thus displacement fields were computed. These displacement fields  
 380 were projected on Williams' series expansion and crack features were extracted. Crack  
 381 features were analyzed qualitatively in cycle with and without overload, then a quan-  
 382 titative analysis based on SVD analysis provides the most interpretable descriptors for  
 383 what occurs during overloading. The main observations can be summarized as follows:

- 384 • *cycle without overload.* in a case of a cycle without overload all features are pro-  
 385 portional thus a single descriptor is required to depict the evolution of the crack  
 386 tip state. In this case we consider  $\delta K_I$ . This observation is consistent with a linear  
 387 behavior of the specimen.
- 388 • *cycle with overload.* In the loading phase (from  $F_{\min}$  to  $F_{\max}$ ) crack features are  
 389 proportional to the load, then they depict a faster increase than load during the  
 390 overloading phase (from  $F_{\max}$  to  $F_{ovl}$ ) making this increase an overload signature.  
 391 The unloading phase is linear with  $\delta F$  and it maintains almost the same slope as  
 392 during the loading phase. The analysis of these crack features shows that a plane  
 393 emanates. We suggested then an SVD analysis to propose an appropriate basis  
 394 of the crack tip state data structure. The first result of this analysis came with  
 395 the fact that  $\delta K_I$  cannot be considered as the unique descriptor of the kinematic  
 396 field. We came out with a non-orthogonal basis of composite features  $(U_f^l, U_f^{nl})$  that  
 397 describes the "linear part" through  $C_t^l$  which vary linearly with respect to  $\delta F$  and  
 398 the "non-linear" part through  $C_t^{nl}$  which is activated only in the overloading phase.

399 These interpretable composite features can be considered as descriptors of the constitu-  
 400 tive behaviour of the crack tip. A clear separation is obtained between the contribution  
 401 to the kinematic fields around the crack tip having linear elastic response with respect

402 to the applied load and its counterpart with a non-linear and non-elastic behaviour.  
403 There is thus all the ingredients to build an effective constitutive model of the crack tip  
404 based on the minimum number of interpretable composite features (linear combination  
405 of Williams' coefficients).

## 406 **Acknowledgments**

407 This research was funded, in whole, by the french national research agency (ANR)  
408 through grant ANR-20-CE08-0017.

## 409 **Declarations**

410 A CC-BY public copyright license has been applied by the authors to the present  
411 document and will be applied to all subsequent versions up to the Author Accepted  
412 Manuscript arising from this submission, in accordance with the grant's open access  
413 conditions.

414 Conflict of interest: The authors declare that they have no conflict of interest



415 **Appendix A Crack features from  $n = 4$  to  $n = 7$**

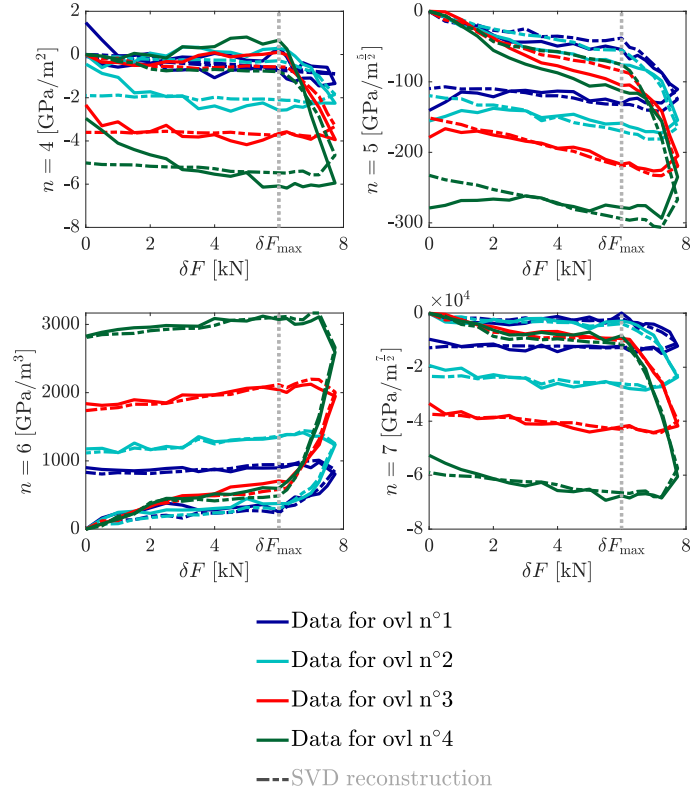


**Fig. A1:** Crack features from  $n = 4$  to  $n = 7$  and their SVD reconstruction ( $\delta \tilde{K}_I$ ,  $\delta \tilde{T}$  and  $\delta \tilde{B}$ ) as a function of  $\delta F$  for cycles with overload

416 **References**

- 417 [1] S. Beden, A. Shahrum, and A. K. Ariffin. Review of Fatigue Crack Propagation  
 418 Models for Metallic Components. *European Journal of Scientific Research*, 2009.  
 419 [2] G. Besnard, F. Hild, and S. Roux. “Finite-Element” Displacement Fields Analysis  
 420 from Digital Images: Application to Portevin–Le Châtelier Bands. *Exp Mech*,

- 421 46(6):789–803, December 2006.
- 422 [3] R. Hamam, F. Hild, and S. Roux. Stress Intensity Factor Gauging by Digital  
423 Image Correlation: Application in Cyclic Fatigue. *Strain*, 43(3):181–192, August  
424 2007.
- 425 [4] C. Henninger, S. Roux, and F. Hild. Enriched kinematic fields of cracked  
426 structures. *International Journal of Solids and Structures*, 47(24):3305–3316,  
427 December 2010.
- 428 [5] R.E. Jones. Fatigue crack growth retardation after single-cycle peak overload in  
429 Ti-6Al-4V Titanium alloy. *Engineering Fracture Mechanics*, 5:585–604, 1973.
- 430 [6] C. Makabe, A. Purnowidodo, and A.J. McEvily. Effects of surface defor-  
431 mation and crack closure on fatigue crack propagation after overloading and  
432 underloading. *International Journal of Fatigue*, 2004.
- 433 [7] P. Paris and F. Erdogan. A Critical Analysis of Crack Propagation Laws. *Journal*  
434 *of Basic Engineering*, 85(4):528–533, December 1963.
- 435 [8] S. Roux and F. Hild. Stress intensity factor measurements from digital image  
436 correlation: post-processing and integrated approaches. *Int J Fract*, 140(1-4):141–  
437 157, July 2006.
- 438 [9] C. Roux-Langlois, A. Gravouil, M.-C. Baietto, J. Réthoré, F. Mathieu, F. Hild,  
439 and S. Roux. DIC identification and X-FEM simulation of fatigue crack growth  
440 based on the Williams’ series. *International Journal of Solids and Structures*,  
441 53:38–47, January 2015.
- 442 [10] J. Réthoré. Automatic crack tip detection and stress intensity factors estimation  
443 of curved cracks from digital images: Automatic crack tip detection and SIF  
444 estimation of curved cracks. *Int. J. Numer. Meth. Engng*, 103(7):516–534, August  
445 2015.
- 446 [11] J. Réthoré. UFreckles, October 2018.
- 447 [12] A. Saxena, J. D. Landes, J. L. Bassani, and W. Nicoletto. *Fatigue crack-tip*  
448 *mechanics in 7075-T6 aluminium alloy from high-sensitivity displacement field*  
449 *measurements. In: Nonlinear fracture mechanics.*, volume 1. ASTM International,  
450 1988. Google-Books-ID: \_X8Epgp8AVsC.
- 451 [13] J. Schijve and D. Broek. The Results of a Test Programme Based on a Gust  
452 Spectrum with Variable Amplitude Loading. *Aircraft Engng*, 34:314–6, 1962.
- 453 [14] D. M. Shuter and W. Geary. Some Aspects of Fatigue Crack Growth Retar-  
454 dation Behaviour Following Tensile Overloads in a Structural Steel. *Fatigue &*  
455 *Fracture of Engineering Materials & Structures*, 19(2-3):185–199, 1996. eprint:  
456 <https://onlinelibrary.wiley.com/doi/pdf/10.1111/j.1460-2695.1996.tb00958.x>.
- 457 [15] S.S.K. Singh, S. Abdullah, and N. Nikabdullah. The needs of understanding  
458 stochastic fatigue failure for the automobile crankshaft: A review. *Engineering*  
459 *Failure Analysis*, 80:464–471, October 2017.
- 460 [16] M. Skorupa, A. Skorupa, J. Schijve, T. Machniewicz, and P. Korbut. Effect of  
461 specimen thickness and stress ratio on fatigue crack growth after a single overload  
462 cycle on structural steel.
- 463 [17] C. Sun, Z. Lei, and Y. Hong. Effects of stress ratio on crack growth rate and  
464 fatigue strength for high cycle and very-high-cycle fatigue of metallic materials.  
465 *Mechanics of Materials*, 69(1):227–236, 2014.

- 466 [18] S. Suresh. Micromechanisms of fatigue crack growth retardation following  
467 overloads. *Engineering Fracture Mechanics*, 18:577–593, 1983.
- 468 [19] C.M. Ward-Close, A.F. Blom, and R.O. Ritchie. Mechanisms associated with  
469 transient fatigue crack growth under variable-amplitude loading: An experimental  
470 and numerical study. *Engineering Fracture Mechanics*, 32(4):613–638, January  
471 1989.
- 472 [20] G. Wild, L. Pollock, A.K. Abdelwahab, and J. Murray. Need for Aerospace  
473 Structural Health Monitoring: A review of aircraft fatigue accidents. *International*  
474 *Journal of Prognostics and Health Management*, 12(3), March 2021.
- 475 [21] M. L. Williams. On the Stress Distribution at the Base of a Stationary Crack.  
476 *Journal of Applied Mechanics*, 24(1):109–114, March 1957.